ACADEMIC PRESS

Available online at www.sciencedirect.com

SCIENCE DIRECT®

Journal of Solid State Chemistry 176 (2003) 234–242

JOURNAL OF SOLID STATE CHEMISTRY

http://elsevier.com/locate/jssc

Molecular dynamics studies of the kinetics of phase changes in clusters III: structures, properties, and crystal nucleation of iron nanoparticle Fe_{331}

Xiaohua Li[a] and Jinfan Huang[b,*]

[a] Department of Chemistry, Nanjing Xiaozhuang College, People's Republic of China
[b] Department of Chemistry, University of Michigan, Ann Arbor, MI 48109, USA

Received 11 May 2003; received in revised form 16 July 2003; accepted 23 July 2003

Abstract

Molecular dynamics (MD) computer simulations have been carried out to study the structures, properties, and crystal nucleation of iron nanoparticles with 331 Fe atoms or with diameter around 2 nm. Structure information for the nanoparticles was analyzed from the MD simulations. Three crystalline phases and one amorphous phase were obtained by cooling the nanoparticles from their molten droplets at different cooling rates or with different lengths of cooling time periods. Molten droplets froze into three different solid phases and a solid–solid transition from a disordered body-centered cubic (BCC) phase to an ordered BCC phase were observed during the slow cooling and the quenching processes. Properties of nanoparticle Fe_{331}, such as melting point, freezing temperature, heat capacity, heat of fusion, heat of crystallization, molar volume, thermal expansion coefficient, and diffusion coefficient, have been estimated. Nucleation rates of crystallization to two solid phases for Fe_{331} at temperatures of 750, 800, and 850 K are presented. Both classical nucleation theory and diffuse interface theory are used to interpret our observed nucleation results. The interfacial free energy and the diffuse interface thickness between the liquid phase and two different solid phases are estimated from these nucleation theories.

Keywords: Iron nanoparticles; Structures; Properties; Crystal nucleation rate; Phase transition

1. Introduction

Iron occurs in three distinct polymorphs (body-centered cubic BCC, δ-BCC, and face-centered cubic FCC) at one atmosphere and in many different phases at high pressure and high temperature. Because iron is one of the most abundant elements on Earth and its application covers all aspects of human lives, the phases of iron and the transitions among different phases of iron have always been subjects of much interest to scientists. For instance, the well-known martensitic transform, which occurs in rapidly cooling the hot steel has been used to harden sword since the ancient Greeks, was seriously studied in late 19th century [1,2]. Nucleation is the early step in a phase transition and it plays an important role in any phase transition study. However, we still lack a reliable quantitative understanding of this step at present [3]. It deserves more studies on this topic, especially for the phase transitions in iron system.

Nucleation study based on particles as small as nanometer size has the advantage of avoiding possible heterogeneous nucleation. Moreover, nanoparticles display novel physical properties and play important roles in modern science and technology. Therefore, we focus our research in the nucleation kinetics of phase transitions based on nanometer size particles [4–12]. Ultra-fine iron particles are expected to have uses in the field of powder metallurgy, magnetic recording, ferrofluids, and water treatment. In this paper, we report our molecular dynamics (MD) simulation [13] results on iron nanoparticles with diameter around 2 nm that contain 331 Fe atoms.

2. Computational experiment procedure

The MD simulations were performed on iron nanoparticles with 331 Fe atoms by an embedded-atom

---

[*] Corresponding author. Fax: +734-647-4865.
E-mail address: jinfanh@umich.edu (J. Huang).

0022-4596/$ - see front matter © 2003 Elsevier Inc. All rights reserved.
doi:10.1016/S0022-4596(03)00414-6

method (EAM) potentials [14a,14b] and by using the program XMD [14c]. No external pressure was used and only the Laplace pressure P_L (which is $2\sigma/r_0$, here σ is the surface tension and r_0 is the radius of the particle) inside the nanoparticles has to be taken into account. Therefore, the systems were quasi-NPT ensembles due to P_L may slightly change during a specific simulation process. Iron atoms were initially arranged in a shape formed by cutting the crystal with a sphere.

A summary of the whole simulation process is given in Fig. 1. The simulations were started at constant temperature with 50,000 time steps in a heat bath of 200 K. A series heating stages then began at 300 K, each succeeding stage is 20°C warmer than the previous one (step 1 in Fig. 1). Every stage was simulated at constant temperature for 50,000 time steps. Heating was continued to 1600 K. To avoid starting from a configuration with evaporated atoms freezing simulations started from 1500 K, each succeeding stage is 20°C cooler than the previous one until the temperature reached 300 K (step 2 in Fig. 1). In all simulations the time step was set to 2 fs. Such a process corresponds to a heating/cooling rate of 2×10^{11} K/s. The molten droplets for the nucleation study were first generated from the heating process mentioned above. After the Fe_{331} particle was melted from the melting process at 1500 K, the heating was continued at 1500 K to form 18 molten droplets each with 50,000 more time steps than the previous one that gave 18 melted systems with different thermal histories for crystal nucleation studies (step 3 in Fig. 1). Nucleation rates were investigated by immediately quenching the melted droplets into a heat bath at the temperatures of interest (step 4–6 in Fig. 1). The highest temperature was chosen at 850 K (step 4 in Fig. 1), above this limit it is difficult to observe crystallization within a reasonable length of simulation time. The lowest temperature was chosen at 750 K (step 6 in Fig. 1), we found droplets are readily frozen into amorphous solid below this temperature. A middle temperature of 800 K (step 5 in Fig. 1) was chosen between these two limits.

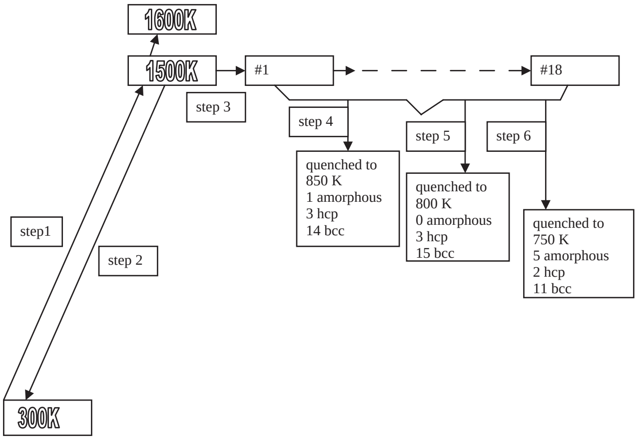

Fig. 1. Flow chart for the simulations performed in this report.

All the heat baths were formed by maintaining the system in an approximate constant temperature through an algorithm that scales the instantaneous velocities in order to bring the temperature to its desired value. Scaling is accomplished by multiplying each particle velocity component by the same factor. To avoid an abrupt temperature change at the beginning of a new temperature the velocities are scaled by 33rd root of the "one step" factor until the system reaches the desired temperature.

The structure information of nanoparticles was obtained from several approaches. Pair correlation curve (or radial distribution curve) provides the information of distances between atoms from which the information about crystal and liquid structures may be derived. Diffraction pattern analysis is the most popular method in determining the structure of bulk crystalline materials. It is also very useful to analyze the structure of crystalline nanoparticles. The scattering intensity of a nanoparticle was calculated from

$$I(s) = f(s)^2 \sum_{i<j} \sin(2\pi s r_{ij})/(2\pi s r_{ij}), \qquad (1)$$

where s is defined as $s = (2\lambda)\sin\theta$ (λ is the wavelength, θ is the Bragg angle), r_{ij} is the distance between atom i and j that can be calculated based on the coordinates of atoms obtained from MD simulations, the f's are the angle-dependent atomic scattering factor. Once the diffraction pattern is obtained, the peak positions are indexed and crystal packing information can be obtained.

The nearest-neighbor distance in the crystalline phase, which can be estimated from the pair correlation curve, is used to determine the cell parameters and the volume of an atom in a crystalline particle. Another method of calculating the average atom volume is to use Voroni polyhedra [15–17] that may be used both for crystalline and liquid nanoparticles. Once the volume of a molecule is obtained, the molar volume, density, and the thermal expansion coefficient can be easily calculated.

Melting, freezing, and other phase transitions usually involve sudden property changes and therefore they can be determined by the sudden slope change on the curves plot properties of the nanoparticles as a function of temperature during the heating or cooling runs or as a function of time during the quenching runs. Caloric curve relating the total energy (E) as a function of temperature has been widely used to determine the melting point and freezing temperature of nanoparticles. This is analogous to the experimental determination by thermal analysis methods. The bond-order parameter method is more sensitive to distinguish the atoms in small particles with an environment of liquidlike or solidlike. The bond-order parameter $\mathbf{q}_{\ell m}$ for atom i is defined by

$$\mathbf{q}_{\ell m}(i) = 1/N_{\mathrm{nb}}(i)\sum_{j=1}^{N_{\mathrm{nb}}(i)} Y_{\ell m}(r_{ij}), \tag{2}$$

where “bond” r_{ij} is a unit vector connecting the atom i with its neighboring atoms j that are within a given radius of cutoff distance from atom i, $N_{\mathrm{nb}}(i)$ is the number of bonds around atom i, and $Y_{\ell m}(r_{ij})$ are the spherical harmonics functions that specify a reference system for the orientation of bond r_{ij}. $Y_{\ell m}(r_{ij})$ can be expressed as

$$Y_{\ell m}(r_{ij}) = Y_{\ell m}(\theta_{ij}, \varphi_{ij}), \tag{3}$$

where θ_{ij} and φ_{ij} are the polar and azimuthal angles of vector r_{ij} in the reference frame. Only when ℓ's are even values spherical harmonics are invariant under inversion. Therefore, the summery in Eq. (2) only consider even ℓ values. Usually a second-order invariant is used to avoid the dependence of the local order parameter on the choice of reference system. The local order parameter $q_\ell(i)$ can be defined by

$$q_\ell(i) = \left[4\pi/(2\ell+1)\sum_{m=-\ell}^{\ell}|q_{\ell m}(i)|^2\right]^{1/2}. \tag{4}$$

By averaging the local order parameter over all the atoms in a nanoparticle we can obtain the global order parameter

$$\mathbf{Q}_\ell = \left[4\pi/(2\ell+1)\sum_{m=-\ell}^{\ell}|Q_{\ell m}|^2\right]^{1/2}, \tag{5}$$

where $\mathbf{Q}_{\ell m}$ is defined by

$$\mathbf{Q}_{\ell m} = \left[\sum_{i=1}^{N} N_{\mathrm{nb}}(i) q_{\ell m}(i)\right] \Big/ \left[\sum_{i=1}^{N} N_{\mathrm{nb}}(i)\right]. \tag{6}$$

The global bond order parameter $\mathbf{Q}_\ell$ depends on the ℓ values and the symmetry of the system. A detailed discussion for the relationship between $\mathbf{Q}_\ell$ values and structure types has been given in Ref. [18] For face-centered cubic (FCC), hexagonal close packed (HCP), icosahedral (Ih), and dechedral (Dh) type structures $\mathbf{Q}_6$ are 0.575, 0.485, 0.663, and 0.430, respectively, which are not very sensitive to different crystal structure type. However, it is close to zero for a liquidlike structure. We will only use $\mathbf{Q}_6$ in this study to monitor the melting and freezing process for Fe_{331} nanoparticles.

The heat capacity is defined by

$$C_p = \left(\frac{\partial E}{\partial T}\right)_p + p\left(\frac{\partial V}{\partial T}\right)_p, \tag{7}$$

where E is the total energy, T is the temperature, V is the volume, and p is the pressure. Therefore, the heat capacity of nanoparticles can be determined from the slope of the caloric curve, the slope of a curve plotting the volume of the nanoparticle as a function of temperature, and the external pressure. The contribution from the second term in condensed materials is trivial. For simplicity, it is reasonable to use the first term only.

Diffusion coefficient of atoms was calculated by following the Einstein relation

$$D = (1/6)(1/t)\langle[r(t) - r(0)]^2\rangle, \tag{8}$$

where D is the diffusion coefficient, t is the time, and r is the position of atoms. The mean square displacement $\langle[r(t) - r(0)]^2\rangle$ for atoms was calculated by

$$\langle[r(t) - r(0)]^2\rangle = (1/N)\sum_{\imath}\langle[r_\imath(t) - r_\imath(0)]^2\rangle, \tag{9}$$

where the average is over as many independent time origins as possible to improve the statistics.

The rate of a homogenous nucleation can be expressed as [19,20]

$$J(T) = A\exp(-\Delta G^*/k_{\mathrm{B}}T), \tag{10}$$

where k_{B} is the Boltzman constant, T is the temperature, and ΔG^* is the free energy barrier to the formation of a critical nucleus of the new phase from the old phase. The differences for the prefactor A and ΔG^* form different nucleation theories. It is assumed that the fraction of unfrozen particles in which a critical nucleus has not yet formed is given by the first-order rate raw

$$N(t)/N_0 = \mathrm{e}^{-JV_{\mathrm{e}}(t-t_0)}, \tag{11}$$

where t_0 is the time lag to achieve a steady state of precritical embryo and V_{e} is the volume of the particle to be effective in nucleation. In a convenient form Eq. (11) can be written as

$$\mathrm{Ln}[N(t)/N_0] = -JV_{\mathrm{e}}(t - t_0). \tag{12}$$

From the slope of the plot $\mathrm{Ln}[N_n(t_n)/N_0]$ vs. t we can obtain the nucleation rate J, where N_0 is the number of total nucleation events studied, and t_n is the time at which the nth nucleation event N_n has taken place.

3. Results

3.1. Melting and freezing

Fig. 2 presents the total energy and the global order parameter Q_6 for Fe_{331} as a function of temperature during the heating and the cooling processes. Selected images generated from the MACSPIN program [21] for heating and cooling processes of Fe_{331} are shown in Fig. 3. It is obvious from Fig. 2 that there is no unique temperature corresponding to the transition due to the extremely high heating rate and the large temperature increment between two successive heating runs. We select the midpoint of a jump on the Caloric curve that occurs during heating of the particle. The uncertainty is estimated from the two temperatures around the

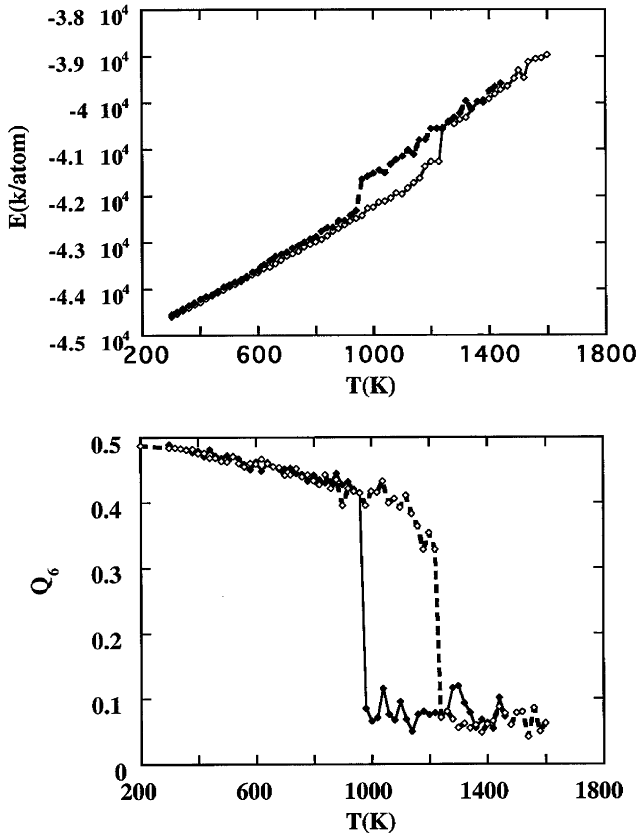

Fig. 2. Total energy per atom and global order parameter as a function of temperature during the heating and the cooling stages. Empty square for Fe_{331} during the heating process. Solid square for Fe_{331} during the cooling process.

midpoint of the jump. According to this definition the melting point and associated uncertainties are 1220(10) K for Fe_{331} under the heating rate mentioned in the previous section. Evaporation was observed after the heating at 1520 K. Therefore, the cooling run for the freezing and nucleation studies was started at 1500 K. Freezing temperature was estimated by following the same definition for the melting point that gives a result of 960(10) K.

Unlike the rock salt nanoparticles where cubic shaped particle is of the most stable shape [9–12], we found spherically shaped iron particle is the most stable one. All the nanoparticles from their molten droplets were frozen into a solid with a shape formed by cutting the lattice with a sphere.

3.2. Phase changes and phases

Fig. 4 plots the energy changes in several quenching runs at 850 K, and diffraction patterns and pair correlation curves selected from certain points on these energy curves are given in Fig. 5 and Fig. 6. Freezing and other phase changes can be seen from the sudden changes on the curves plotted in Fig. 4.

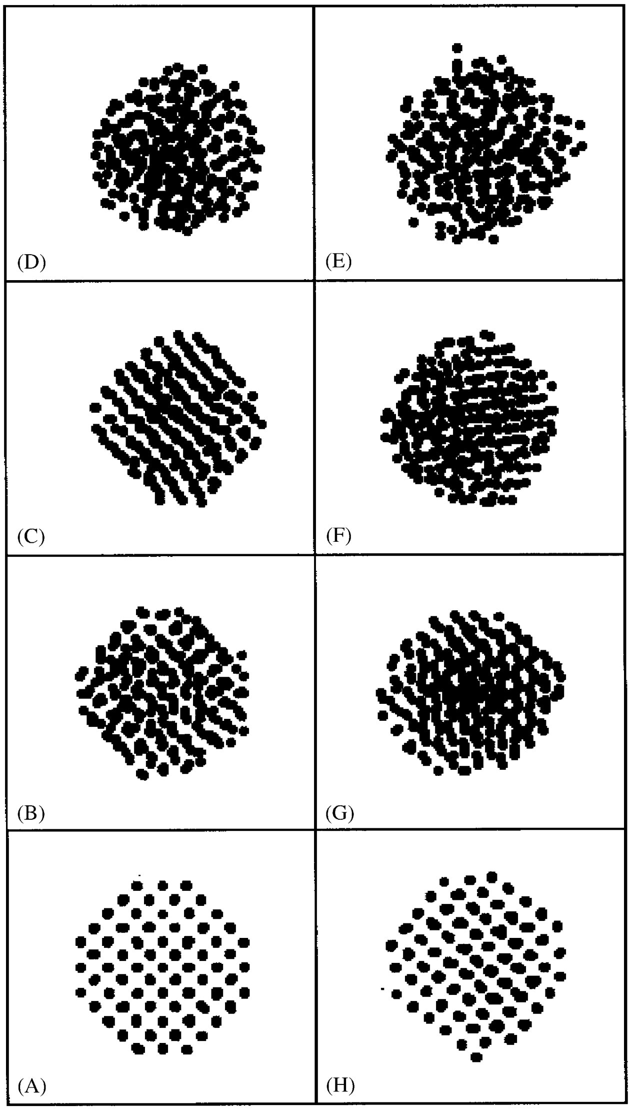

Fig. 3. Snapshot images of nanoparticles at various stages of heating and cooling. Left-hand figures are for heating at: (A) 300 K, (B) 920 K, (C) 1100 K, and (D) 1300 K; Right-hand figures are for cooling at: (E) 1500 K, (F) 1000 K, (G) 700 K, and (H) 300 K.

When a molten liquid droplet was quenched from 1500 to 850 K it immediately became a supercooled liquid. The big drop in kinetic energy for this step resulted in the huge total energy change at the beginning of all the curves given in Fig. 4.

The supercooled liquid nanoparticle shown in curve A of Fig. 4 lasted for about 2300 ps, then the droplet slowly froze into a solid. The solid phase formed in this process is more like an amorphous phase based on the diffraction pattern given in curve B of Fig. 5 and the pair correlation curve B of Fig. 6. Six similar phase transition events were observed in the 54 quenching runs that indicates a liquid to an amorphous solid phase transition really exists in this system. Five out of six of this type transition were observed when the molten

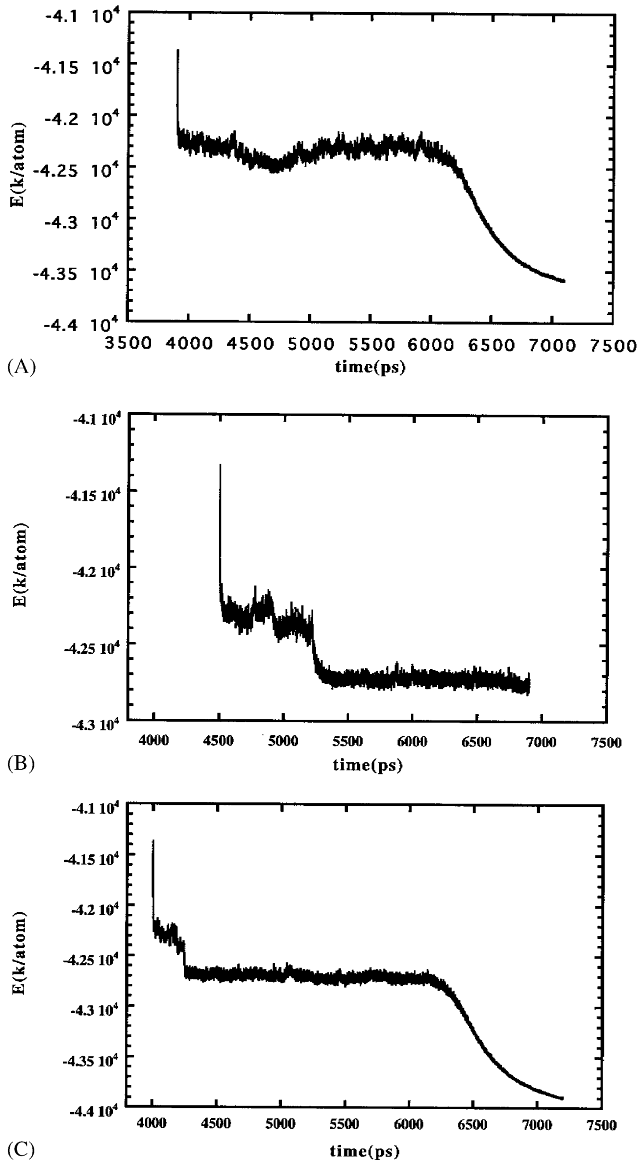

Fig. 4. Typical energy evolution curves for molten nanoparticles quenching to 850 K. (A) The pattern froze from the liquid to the amorphous solid; (B) the pattern froze from the liquid to the HCP solid; and (C) the pattern froze from the liquid to the disordered BCC solid and then the disordered BCC transferred to the ordered BCC solid.

droplets were quenched into the bath of 750 K that indicates this phase is more easy to form under deeper supercooling condition.

Curve B of Fig. 4 gives another type of phase transition observed. After the supercooled liquid droplet soaked in the heat bath of 850 K for about 700 ps a fast phase transition started which gives a sharp drop on the energy curve. The solid phase identified from curve C of Fig. 5 and curve C of Fig. 6 is more likely a HCP solid. Eight similar phase transitions were observed in the 54 quenching runs, 2 from 750 K, 3 from 800 K, and 3 from 850 K.

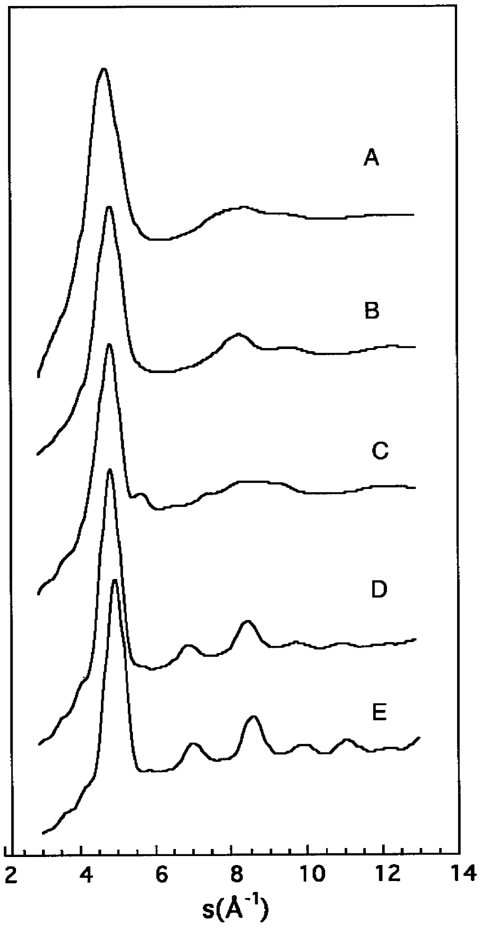

Fig. 5. Diffraction patterns for different phases. (A) From supercooled liquid at 1200 K; (B) from the amorphous solid at 850 K (structure from the last point of curve A in Fig. 4); (C) from the HCP solid at 850 K (structure from the last point of curve B in Fig. 4); (D) from the disordered BCC solid at 850 K (structure from the middle point of curve C in Fig. 4); and (E) from the ordered BCC solid at 850 K (structure from the last point of curve C in Fig. 4).

Curve C of Fig. 4 shows a liquid-to-solid transition and a solid-to-solid phase transition. Shortly after the supercooled droplet sat in the heat bath of 850 K, it is frozen into a disordered BCC solid (see curve D of Fig. 5 and curve D of Fig. 6). A slow solid–solid transition started after another 2000 ps. The solid formed in the second step is an ordered BCC phase based on the diffraction pattern plotted in curve E of Fig. 5 and pair correlation curve E of Fig. 6. The ordered BCC phase is also the phase observed from the cooling process at the rate of 2×10^{11} K/s. Hereafter we will call this phase as ordered BCC phase.

3.3. Properties and nucleation of crystallization

The calculated properties for Fe_{331} nanoparticles are summarized in Table 1. Fig. 7 plots the $\ln[N_n(t_n)/N_0]$ vs. time t_n obtained from quenching runs for the liquid froze to disordered BCC phase of Fe_{331} at different temperatures. Based on the assumption that takes the total volume of a nanodroplet as the effective volume V_e and all the droplets form single crystals, the calculated nucleation rates are listed in Table 2. Uncertainties are standard deviations based solely on the counting statistics [22]

$$\sigma_\tau/\tau = 1.10(N_0 - 3)^{1/2}, \tag{13}$$

where τ is the measured property and σ_τ is the uncertainty of τ.

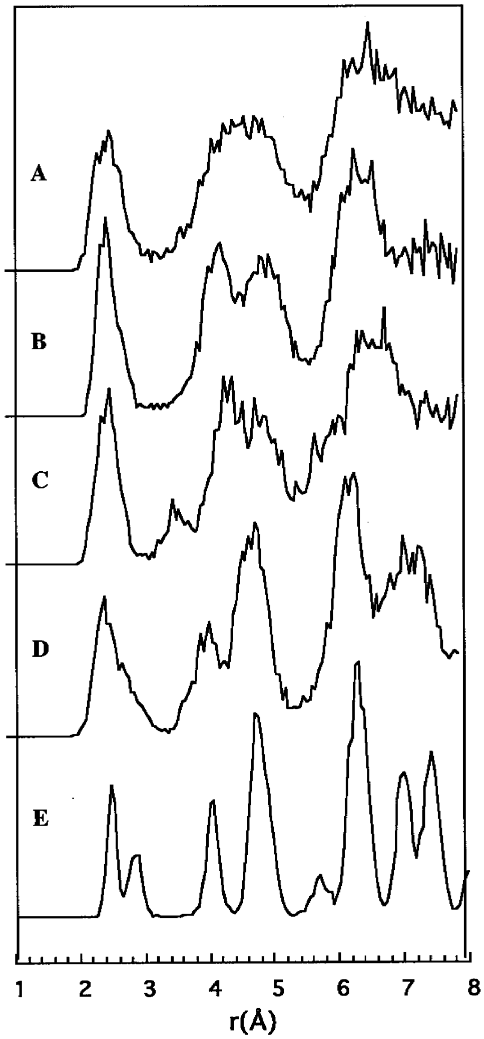

Fig. 6. Pair correlation curves for different phases: (A) from supercooled liquid at 1200 K; (B) from the amorphous solid at 850 K (structure from the last point of curve A in Fig. 4); (C) from the HCP solid at 850 K (structure from the last point of curve B in Fig. 4); (D) from the disordered BCC solid at 850 K (structure from the middle point of curve C in Fig. 4); and (E) from the ordered BCC solid at 850 K (structure from the last point of curve C in Fig. 4).

4. Discussion

4.1. Brief structure information about different phases of Fe_{331} nanoparticles

The amorphous iron fine particle sample has been prepared from sonochemical synthesis experimentally

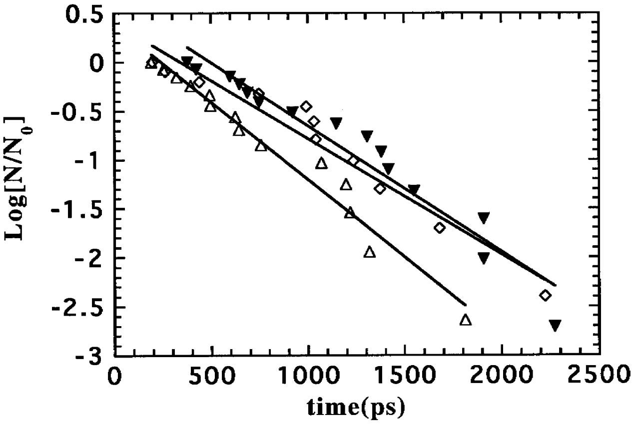

Fig. 7. $\ln[N_n(t)/N_0] \sim t$ plot selected from 54 MD runs on Fe_{331} that forms the disordered BCC phase. Empty triangles are from 750 K. Filled triangles are from 800 K. Empty squares are from 850 K.

Table 2
Calculated nucleation rate (m^{-3}/s)

Phase transition	750 K	800 K	850 K
L-HCP		$5.3(1.7) \times 10^{35}$	$2.0(0.5) \times 10^{35}$
L-BCC1	$3.0(0.9) \times 10^{35}$	$3.3(1.0) \times 10^{35}$	$4.0(1.2) \times 10^{35}$

[a] L: liquid; HCP: hexagonal close packing; BCC1:disordered body-centered cubic.

Table 1
Calculated properties of Fe_{331} nanoparticles

Property	State	Temperature rage	Value or expression
Volume ($\times 10^{-6}$ m^3/mol)	Solid	300–1220 K	$6.94 \times 10^{-6} + 3.293 \times 10^{-10}$ T
	Liquid	1100–1600K	$6.68 \times 10^{-6} + 6.77 \times 10^{-10}$ T
Thermal expansion coefficient (1/K)	Solid	300 K	2.21×10^{-5}
	Liquid	1100 K	4.54×10^{-5}
Heat capacity (J/mol K)	Solid	300–1220K	28.0
	Liquid	960–1600 K	37.4
Heat of fusion (KJ/mol)	Solid to liquid	At 1220 K	5.74
Heat of crystallization (KJ/mol)	Liquid to solid	At 960 K	5.59
Diffusion coefficient (m^2/s)	Liquid	1000–1500 K	3.67×10^{-8} exp(−41,405/RT)

[23]. However, no diffraction peaks were observed on the samples from powder X-ray diffraction. Only a diffuse ring characteristic of an amorphous metal was obtained from the electron micro diffraction with a transmission electron microscope. This result is very similar to the diffraction pattern plotted in curve B of Fig. 5. Compared with the pair correlation curve for supercooled liquid (curve A of Fig. 6) we can see the distribution of the first closest distance between atoms in this phase (curve B of Fig. 6) is slightly narrower than that in the supercooled liquid, while the peak corresponding to the second closest distance starts to separate into two peaks.

Instead of getting an FCC phase that is observed under normal pressure, we got a phase most likely a HCP phase that usually obtained from the high pressure and high temperature condition. It is understandable because the high Laplace pressure on small particles is expected. Comparing with other phases obtained from our results, a distance of ~3.5 Å between atoms is the unique character of this phase. The analysis of the coordinates for this phase reveals that it is the mixture of different packing structures. The nanoparticles in this phase have an average composition of 10% FCC, 55% HCP, 20% Dh, 1% Ih, and 14% BCC.

As shown from curves D and E of Fig. 5, both disordered BCC and ordered BCC phases give similar diffraction pattern. The analysis of the coordinates for these two phases show 100% BCC packing. The existence of these two different phases can be confirmed from the energy–time curve given in curve C of Fig. 4 and the pair correlation curves D and E in Fig. 6.

Disordering is the common character for all the solid phases obtained in this study, especially on the surface. Even the phase we called ordered BCC still has certain degree of disordering compared with a perfect BCC packed nanoparticle. From the pair correlation curve E in Fig. 6 for the ordered BCC, it is obvious that even the peaks corresponding to the shortest distance $(3/2)^{1/2}a$ and the second shortest distance (a) are not completely separated, where a is the cell dimension. The peak around 5 Å that contains distances $(11/2)^{1/2}a$ and $(3)^{1/2}a$ and the peak around 6.3 Å that contains distances $(19/4)^{1/2}a$ and $(5)^{1/2}a$ cannot even show the separations. In the disordered BCC, the separation for these peaks gets even worse. The missing of the peak at $2a$(5.85 Å) in disordered BCC phase suggests the possible superlattice/sublattice relationship between the ordered BCC and disordered BCC or the disordered BCC phase is actually a phase with a symmetry slightly lower than the ordered BCC phase. Detailed structure analysis for all the phases are in progress and will be reported in a forthcoming paper.

4.2. Properties of Fe_{331} nanoparticles

One important development in recent nanostructure materials research is that the properties (electrical, optical, chemical, mechanical, magnetic, etc.) of nanoparticles can be selectively controlled by engineering the size, morphology, and composition of the particles. After developing materials in this near-atomic size range, engineers can incorporate them into other materials, exploiting the properties of the nanoparticle surface atoms to create new combined materials with enhanced or entirely different properties from their parent materials. A particular property of interest is the melting point of nanoparticles due to the nano-fabrication of metal surface. Usually melting point reduction is not really significant until the particle size is less than about 20 nm. For instance, the melting point of bulk tin is 232°C, then falls to 213°C and 160°C, respectively, for 20 and 10 nm particles [24]. In a purely adiabatic situation, we should be able to melt and attach metal nanoparticles to the surface at temperatures below bulk melting points. However, the re-melt temperature would represent bulk metal, so it would not wet and flow unless above the melting point of bulk metal. The iron surface with nanoparticles fabricated has very high resistance to corrosions. The melting point of Fe_{331} (~2 nm in diameter) is about 0.67 of the experimental bulk melting point of 1811 K, the ratio is much lower than that of tin (0.86 for 10 nm particles). It might be an interesting reference data for the surface nano-fabrication of iron.

The calculated molar volume for solid is slightly smaller than the experimental bulk molar volume. For instance, the calculated molar volume of solid nanoparticles at 298 K is $7.04 \times 10^{-6}\,\mathrm{m^3/mol}$, while the experimental result for bulk crystal is $7.09 \times 10^{-6}\,\mathrm{m^3/mol}$ [25]. It is difficult to tell whether this discrepancy comes from the potential function used in the simulation or whether it is real. However, the thermal expansion derived from the temperature dependence of volume is consistent with our result for KI nanoparticles. It was observed that in KI nanoparticles, the calculated thermal expansion coefficients of nanocrystals are larger than that of the bulk. [10] This character of nanoparticles is mainly due to the high percentage surface atoms in nanoparticles. In present case, one comparison can be made with experimental data is that the calculated linear thermal expansion coefficient for crystalline iron nanoparticles is $1.46 \times 10^{-5}\,\mathrm{K^{-1}}$ at 273 K, while the value from experiment for bulk is $1.176 \times 10^{-5}\,\mathrm{K^{-1}}$ at this temperature [25].

The MD simulation allows us to get the molar volume of deeply supercooled liquid droplets where the nucleation of crystallization will be studied. There is no experimental data available in such a supercooled condition. The main interest to calculate the molar volume or density for nanoparticles here is to estimate the density difference between the supercooled liquid and the solid for the purpose of calculating the Laplace pressure effect during the nucleation process. Usually we estimate this difference by extrapolating from the bulk density. If the temperature dependence of the liquid density is available the extrapolation from the bulk liquid at most provides us some information about the molar volume in the core of a nanodroplet. As we recently noticed many of the critical nuclei formed near the surface layers and therefore it is necessary to take into account all nanodroplets, not just the core. We hope the molar volume estimated from our current method is more proper for this purpose because we are dealing with problems under the same potential function and the error may be systematically cancelled.

The heat capacity value of 28.0 J/mol K of solid nanocrystal Fe_{331} is higher than the value of 24.64 J/mol K for bulk solid [25] that may also relate to the surface energy for the small particles. A study to check the size dependence of heat capacity may be necessary to understand this result. As expected the calculated heat of fusion and heat of crystallization for the nanoparticles are much smaller than that of the bulk due to the surface energy.

4.3. *Nucleation of crystallization*

The rate of nucleation of crystallization from molten liquid droplets to the disordered BCC has the tendency to increase with increase in nucleation temperature, while the rate for freezing to the HCP phase has an opposite tendency. Due to the large uncertainties with the observed nucleation rates, especially very few nucleation events observed for the HCP phase, such a comparison is made solely neglecting the uncertainties.

Although the rate to HCP is higher than that to the disordered BCC at 800 K, 15 out of 18 events froze to the disordered BCC. This is due to the shorter nucleation time lag in the case that froze to the disordered BCC phase. Unfortunately, the lack of viscosity data in the supercooled liquid iron for different phases prevents us from estimating the nucleation time lag at moment.

To understand the nucleation results from our study, we tried applying different nucleation theories. Both CNT [19,20] and DIT [26–29] can be used to interpret our observed results. The details of these theories have been summarized in our previous papers [11,12].

The application of CNT allows us to get the interfacial free energy between the phase transforms from and the phase transforms to in the phase transition. In the crystallization case the interfacial free energy between the liquid and the solid can be estimated from the observed nucleation rate. This property is usually very difficult to measure directly from experiments. As shown in Table 3 at the same temperature, the interfacial free energy between the liquid and different solid phases is different. At the same temperature the interfacial free energy between the liquid and the disordered BCC phase is lower than that from the liquid and the HCP interface.

Table 3
Interfacial free energy and diffuse interface thickness[a]

T/Cluster	CNT	DIT
	σ_{sl}	δ
750 K		
L-BCC1	0.1010	0.48
800 K		
L-HCP	0.0870	0.42
L-BCC1	0.0790	0.38
850 K		
L-HCP	0.0720	0.39
L-BCC1	0.0700	0.38

[a] The unit for σ_{sl} is in J/m^2, and δ is in Å.

The temperature dependence of the interfacial free energy for the liquid and the disordered BCC boundary from CNT presented in Table 3 can be fitted into a widely used equation

$$\sigma_{sl}(T) = \sigma_{sl}(T_1)(T/T_1)^n, \tag{14}$$

where value of −2.9 for n in the temperature range from 750 to 850 K was obtained. Nucleation data for the freezing of mercury give a value of ~0.3 to 0.4 for n [30]. It is interesting to see the n value for Fe_{331} is a negative value in this temperature range. We noticed that the interfacial free energy between the liquid and the disordered BCC decreases with increase in temperature in the temperature range 750–850 K. If we rewrite Eq. (14) as

$$\sigma_{sl}(T) = \sigma_{sl}(T_1)(T_1/T)^n \tag{15}$$

that will result in an n value of 0.34.

One important property that can be obtained from the DIT is the diffuse interface thickness δ. The diffuse interface thickness δ parameter for the boundary between the liquid and different solid phases derived from DIT with our nucleation rates is also different at the same temperature. It is smaller for the boundary between the liquid and the disordered BCC comparing with that for the liquid–HCP interface. Temperature dependence only can be estimated for the liquid–disordered BCC boundary. It can be approximately described by an equation similar to Eq. (15) with the m value of −1.83.

$$\delta(T) = \delta(T_1)(T_1/T)^m. \tag{16}$$

According to Granasy [26] the δ value can be used to estimate the structure factor k_t. The relationship between the δ and the structure factor k_t is

$$k_t = \delta v_m^{-1/3}, \tag{17}$$

where v_m is the volume of an atom. It leads to a k_t value of 0.003 from Eq. (17) if we use the v_m value of

$12.45 \times 10^{-30}\,\mathrm{m}^3$ for an atom in the liquid and the δ value of 0.006 Å at the melting point derived from Eq. (16). For a series of metalloids the k_t value was found to be ~ 0.32 [31], while for metals the value of 0.45 was used [31]. The k_t value of 0.003 obtained from Fe_{331} is surprisingly too small which indicates that the temperature dependence of δ given in Eq. (16) may not be extended to the bulk melting temperature. Same conclusion may be true for the temperature dependence of the interfacial free energy given in Eq. (14). In sodium chloride system we found nucleation rate decreases with increase in the temperature above 450 K [8,9]. However, it should increase with increase in the temperature based on both CNT and DIT under 450 K [32]. It seems very likely that we may have similar trend in iron system and we got the information only in the low temperature end. Therefore, further studies in higher temperature range with larger particles will be necessary to extrapolate the result to bulk materials.

5. Concluding remarks

MD computer simulation on nanoparticles of Fe_{331} shows very interesting structure, property, and phase transition information. Four different solid phases, an amorphous phase, an HCP phase, a disordered BCC phase, and an ordered BCC phase, are identified. Properties of the nanoparticles Fe_{331} are found apparently different from that of the bulk. Lower melting point, larger thermal expansion coefficients, larger heat capacity, and lower latent energy of melting and freezing for Fe_{331} are consistent with the results we obtained from other systems. The majority product of the crystallization when the nanopaticles rapidly cooled from the molten droplets is the disordered BCC phase. Nucleation rates of crystallization to this phase are $3.0(0.9) \times 1035$, $3.3(1.0) \times 1035$, and $4.0(1.2) \times 1035\,\mathrm{m}^{-3}/\mathrm{s}$ at 750, 800, and 850 K, respectively. Interfacial free energy between the liquid and this solid phase, σ_{sl}, estimated form CNT are 0.101 (at 750 K), 0.079 (at 800 K), and 0.070 (at 850 K) $\mathrm{J/m}^2$. The extrapolation of the interfacial free energy and the diffuse interface thickness to higher temperature range indicates that we got the information at the low temperature end only.

All the results described here are based on the potential we cited. Further studies with different potential functions, number of nucleation events used, and the thermal history of the molten systems are being carried out and will be reported in a forthcoming paper.

Acknowledgments

This work was supported by a grant from Nanjing Xiaozhuang College of P.R. China for Xiaohua Li and a grant from the National Science Foundation of USA to the University of Michigan.

References

[1] C.M. Wayman, H.K. Bhadeshia, in: R.W. Cahn, P. Hassen (Eds.), Physical Metallurgy, Vol. 2, North-Holland, Amsterdam, 1996 (Chapter 15).
[2] L. Delaey, in: R.W. Cahn, P. Hassen, E.J. Kramer (Eds.), Phase Transformations in Materials, Vol. 5, VCH, Weinheim, Germany, 1991, pp. 339–404.
[3] J.M. McBride, Science 256 (1992) 814.
[4] J. Huang, L.S. Bartell, J. Phys. Chem. 98 (1994) 4543.
[5] J. Huang, L.S. Bartell, J. Phys. Chem. 99 (1995) 3924.
[6] J. Huang, W. Lu, L.S. Bartell, J. Phys. Chem. 99 (1995) 11147.
[7] J. Huang, W. Lu, L.S. Bartell, J. Phys. Chem. 100 (1996) 14276.
[8] J. Huang, X. Zhu, L.S. Bartell, J. Phys. Chem. A 102 (1998) 2708.
[9] L.S. Bartell, J. Huang, J. Phys. Chem. A 102 (1998) 8722.
[10] J. Huang, L.S. Bartell, J. Mol. Struct. 567 (2001) 145.
[11] H. Deng, J. Huang, J. Solid State Chem. 159 (2001) 10.
[12] M. Ma, W. Lu, J. Huang, J. Solid State Chem. 165 (2002) 289.
[13] J.M. Haile, Molecular Dynamics Simulation: Elementary Methods, Wiley-Interscience, New York, 1997.
[14] (a) M.S. Daw, S.M. Foiles, M.I. Baskes, Mater. Sci. Rep. 9 (1993) 251;
(b) D. Farkas, Potential data for iron, http://www.ims.uccon.edu/centers/simul/pot/fefarkas.pot;
(c) J. Rifkin, XMD program, jon.rifkin@uconn.edu at the University of Connecticut.
[15] M. Tanemura, Y. Hiwatari, T. Ogawa, N. Ogita, A. Ueda, Prog. Theor. Phys. 58 (1977) 1079.
[16] C.S. Hsu, A. Rahman, J. Chem. Phys. 71 (1979) 4974.
[17] J.N. Cape, J.L. Finney, L.V. Woodstock, J. Chem. Phys. 75 (1981) 2366.
[18] Y.G. Chushak, L.S. Bartell, J. Phys. Chem. B 105 (2001) 11605.
[19] D. Turnbull, J.C. Fisher, J. Chem. Phys. 17 (1949) 71.
[20] E.R. Buckle, Proc. Roy. Soc. London A 261 (1961) 189;
E.R. Buckle, Proc. Roy. Soc. London A 261 (1961) 197.
[21] MacSpin 3.01, Abacus Concepts, Inc., Austin, TX, 1991.
[22] Y. Chushak, P. SantiKary, L.S. Bartell, J. Phys. Chem. A 103 (1999) 5636.
[23] K. Suslick, S. Choe, A. Cichowlas, M. Grinstaff, Nature 353 (1991) 414.
[24] C.R.M. Wronski, Br. J. Appl. Phys. 18 (1967) 1731.
[25] Data from the website http://environmentalchemistry.com/yogi/periodic/Fe.html
[26] L. Granasy, Mater. Sci. Eng. A 178 (1994) 121.
[27] L. Granasy, Europhys. Lett. 24 (1993) 121.
[28] L. Granasy, J. Non-Cryst. Solids 162 (1993) 301.
[29] L. Granasy, J. Phys. Chem. 99 (1995) 14183.
[30] D. Turnbull, J. Chem. Phys. 20 (1952) 411.
[31] D. Turnbull, J. Appl. Phys. 21 (1950) 1022.
[32] J. Huang, L.S. Bartell, J. Phys. Chem. A, submitted for publication.